

# Raman spectroscopy of femtosecond multi-pulse irradiation of vitreous silica: experiment and simulation

N.S. Shcheblanov,<sup>1,\*</sup> M.E. Povarnitsyn,<sup>2,†</sup> K.N. Mishchik,<sup>3,‡</sup> and A. Tanguy<sup>4,§</sup>

<sup>1</sup>*Centre de Physique Théorique, CNRS & Laboratoire des Solides Irradiés CEA-CNRS, Ecole Polytechnique, F-91128 Palaiseau, France*

<sup>2</sup>*Joint Institute for High Temperatures, RAS, 13 Bld. 2 Izhorskaya str., 125412 Moscow, Russia*

<sup>3</sup>*Amplitude Systèmes, 11 avenue de Canteranne, Cité de la Photonique, F-33600 Pessac, France*

<sup>4</sup>*Université de Lyon, LaMCoS, INSA-Lyon, CNRS UMR5259, F-69621 Villeurbanne Cedex, France*

(Dated: October 4, 2017)

We report an experimental and numerical study of femtosecond multi-pulse laser-induced densification in vitreous silica ( $v\text{-SiO}_2$ ) and its signature in Raman spectra. We compare the experimental findings to recently developed molecular dynamics (MD) approach accounting for bond-breaking due to laser irradiation, together with a dynamical matrix approach and bond polarizability model based on first-principle calculations for the estimation of Raman spectra. We observe two stages of the laser-induced densification and Raman spectrum evolution: growth during several hundreds of pulses followed by further saturation. At the medium-range, the network connectivity change in  $v\text{-SiO}_2$  is expressed in reduction of the major ring fractions leading to more compacted structure. With the help of Sen & Thorpe model, we also study the short-range order transformation and derive the interbonding Si–O–Si angle change from the Raman measurements. Experimental findings are in excellent agreement with our MD simulations, and, hence, support bond-breaking mechanism of laser-induced densification. Thus, our modeling explains well the laser-induced changes both in the short-range order caused by the appearance of Si-coordination defects and medium-range order connected to evolution of the ring distribution. Finally, our findings disclose similarities between sheared-, permanently-densified- and laser-induced-glass and suggest interesting future experiment in order to clarify the impact of the thermo-mechanical history on glasses under shear, cold- and hot-compression, and laser-induced densification.

## I. INTRODUCTION

Comprehension of the processes of laser-induced modification in vitreous silica ( $v\text{-SiO}_2$ ) and their control remains an important research issue. This concerns the accurate design of the optical properties via local laser-induced refractive index changes (RIC), serving in the fabrication of embedded optical components in fibers and bulk materials [1–3]. The densification of  $v\text{-SiO}_2$  due to laser irradiation seems reasonable to cause a uniform RIC [4, 5]. The supporting evidence of this mechanism was provided by micro-Raman spectroscopy for both single- [6, 7] and multi-pulse [8–14] experiments.

In these experiments, the analyzes were mainly focused on the strongest band ( $\sim 437\text{ cm}^{-1}$ ) and defects lines  $D_1$  and  $D_2$  ( $\sim 495\text{ cm}^{-1}$  and  $\sim 606\text{ cm}^{-1}$ ), usually related to four-membered and three-membered rings (or 4- and 3-fold), respectively. Analysis in terms of 3- and 4-fold rings is still a topic of discussion [15–17]. It was shown an increase of the intensity of the  $D_2$  band, together with a stagnation of the  $D_1$  band (in opposition with cold compressed glasses). In Ref. [5], we treated the hypothesis of the bond-breaking mechanism leading to  $v\text{-SiO}_2$  densification under laser irradiation. We addressed to the

medium-range order and explained well the behavior of defect line  $D_2$  relying on the connection between population of the 3-fold rings and  $D_2$  lines. However, all these previous Raman measurements indicating material sensitivity to laser irradiation were not compared to numerical Raman results [9, 11, 14, 18] and no Raman data are available for successive laser-induced experiments in the high-frequency range ( $\sim 900\text{--}1300\text{ cm}^{-1}$ ).

In parallel, intensive studies of  $v\text{-SiO}_2$  glass are continuing aimed at studying the role of thermo-mechanical history in densification [19–21] and plastic-shear [22] where, in particular, it is observed a specific sensitivity of Raman spectra in the high-frequency range. In order to infer structural information from Raman spectra in silica glasses, the Sen and Thorpe (ST) analysis [23] relating the position of the characteristic bands to interbonding angle is usually applied [24, 25].

Here, we present a systematic analysis of the effect of multi-pulse femtosecond laser on vibrational properties, Raman spectra, medium-range and short-range structure, with the help of numerical calculations compared to experimental measurements of Raman spectra.

## II. METHODS

### A. Experiment

The sketch in Fig. 1 shows a multiscale nature of the writing processes involved in the consideration. Fem-

\* nikita.shcheblanov@polytechnique.edu

† povar@ihed.ras.ru

‡ kmishchik@amplitude-systemes.com

§ anne.tanguy@insa-lyon.fr

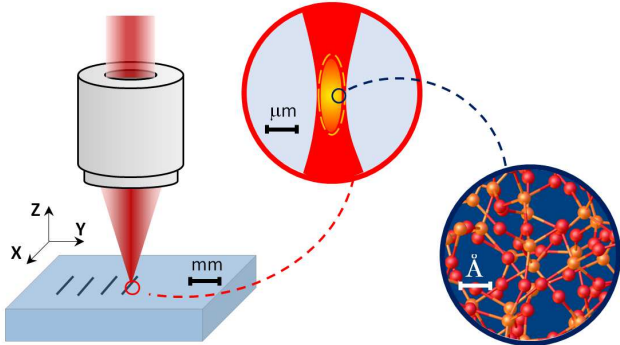


FIG. 1. Schematic representation of the femtosecond laser writing. At macro-scale, the laser beam is focused inside the bulk of  $v$ -SiO<sub>2</sub> via objective. At micro-scale, photoionization conditions are realized in the focal area. At nano-scale, the structure of  $v$ -SiO<sub>2</sub> is composed of network-forming species Si (orange) and O (red) undergoing bond-breaking due to photoionization.

tosecond laser pulses are produced by a regeneratively amplified Ti:sapphire laser system at 800 nm with a nominal pulse duration  $\tau_p = 130$  fs (FWHM) and an energy  $1 \mu\text{J}$ . The long working distance  $20\times$  microscope objective (Mitutoyo MPlan,  $\text{NA} = 0.42$ ,  $f = 10$  mm) is employed to focus the ultrashort laser pulses into the bulk of silica [10]. A laser beam diameter is less than the objective pupil ( $d = 5$  mm at the level  $1/e^2$ ), therefore the nominal value of NA is corrected to  $\text{NA}_{\text{eff}} = 0.3$ . Polished high-purity synthetic fused silica (Corning 7980-5F, 800-1000 ppm concentration of OH impurities) samples are mounted on a XYZ motion stage. Translation parallel to the laser propagation axis allows to write long waveguiding structures produced with controlled number of pulses. The modifications are produced at 10 kHz laser repetition rate, when the material is thermally relaxed before the new pulse arrival. This is in agreement with other reports indicating that heat accumulation effect in silica plays an important role only at MHz regime of irradiation [26].

Laser modification results in a uniform positive refractive index changes of exposed volume (type I structures [27]), that is confirmed by the waveguiding properties of the written structures and additionally verified using phase contrast microscopy. The Raman spectra of the irradiated samples are recorded with a Horiba Jobin Yvon confocal micro-spectrometer in a backscattering configuration. The laser excitation is performed using a HeCd source at 442 nm wavelength. The arrangement allows for a spatial resolution better than  $1 \mu\text{m}$  and a spectral resolution of  $3 \text{ cm}^{-1}$ .

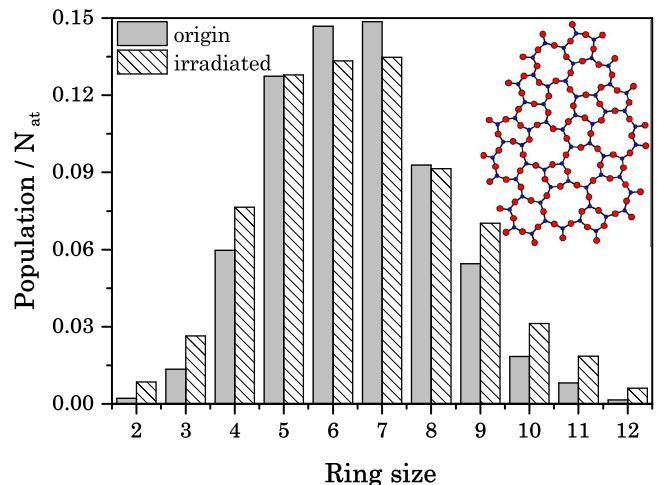


FIG. 2. Evolution in the distribution of rings in  $v$ -SiO<sub>2</sub>. Grey shaded distribution corresponds to origin samples. Patterned distribution corresponds to samples irradiated by 800 pulses. The results of modeling are obtained by averaging over 10 samples. Number of atoms:  $N_{\text{at}} = 8232$ . Inset: Two-dimensional schematic diagram of the  $v$ -SiO<sub>2</sub> network with added colors [28].

## B. MD simulation

In our study, the  $v$ -SiO<sub>2</sub> model is prepared following the work [29]. A system of 8232 atoms (size  $\sim 5$  nm) is obtained within molecular dynamics (MD) simulation (via *LAMMPS* [30]) using a melt-quench procedure [31], and the quenching rate is  $5.2 \times 10^{13} \text{ K}\cdot\text{s}^{-1}$ . The equilibration of the liquid, quench and relaxation of the glass are performed classically using the BKS potential [32] modified by Carré *et al.* [33] (see Appendix A). By evolving the model during 10, 20...100 ns at liquid stage, we obtain 10  $v$ -SiO<sub>2</sub> samples at density of  $2.2 \text{ g}\cdot\text{cm}^{-3}$ .

In order to consider the interaction of sub-picosecond laser pulses with  $v$ -SiO<sub>2</sub> we introduced a bond-breaking mechanism into the MD scheme [5]. The whole simulation cycle of a laser pulse interaction with an MD glass model is as follows. The simulation starts from an instantaneous generation of broken bonds emulating the laser pulse excitation stage. The ionization degree is 0.018%, corresponding to two broken bonds per sample (or free electron density  $1.6 \times 10^{19} \text{ cm}^{-3}$ ). At the second step, the excited electrons transfer energy to the atomic system heating the sample. The temperature saturates with time reaching the maximum value (500 K). Therefore, we evolve our glass sample during the next 5 ps at 500 K. Subsequently, at the third step, a cooling to the room temperature, 300 K, occurs during 100 ps. At the end of the cooling stage, we repair instantly an interaction ability for previously bond-broken Si- and O-atoms. Finally, an annealing at room temperature is applied. We repeat this cycle a required number of times to simulate multi-pulse laser irradiation (up to 1000 pulses).

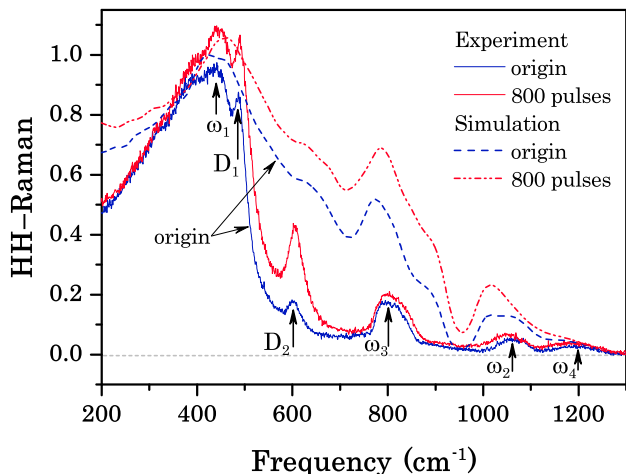


FIG. 3. HH-Raman spectra in  $v$ -SiO<sub>2</sub>. Experimental data: origin sample — solid blue, after irradiation — solid red. The simulation results: origin — dashed blue, after irradiation — solid dash-dot red. The results of simulation are averaged over 10 configurations. Reference frequencies discussed in the text are  $\omega_1 = 437$  cm<sup>-1</sup>,  $\omega_3 = 800$  cm<sup>-1</sup>,  $\omega_2 = 1060$  cm<sup>-1</sup>,  $\omega_4 = 1200$  cm<sup>-1</sup>.

### C. Raman model

In our previous study we established that the laser-induced densification of  $v$ -SiO<sub>2</sub> is traced to medium-range changes in topology of the atomic network. These changes consist in an increase of network connectivity caused by the reduction of major ring fractions of six- and seven-membered rings to minor fractions of three- and four-membered rings [5]. In Fig. 2 we show the evolution in the distribution of rings in  $v$ -SiO<sub>2</sub> upon multi-pulse irradiation. However, it is impossible to directly extract ring statistics or local ring environments in the bulk from experimental measurements. Nonetheless, by applying the Raman spectroscopy enabling to perform the vibrational analysis at  $\mu$ m-scale we can infer the information at medium-range and short-range order.

Here, we briefly outline the formulation that we use for the calculation of Raman activities. We focus only on first-order processes, which involve a single phonon excitation. In the Stokes process, in which a vibrational excitation is created by an incoming photon, we express the total power cross-section as (in esu units) [34]:

$$\mathcal{I}^P(\omega) = \frac{2\pi\hbar}{\omega} \frac{g(\omega)(\omega_L - \omega)^4}{V^{-1}c^4} \sum_n \mathcal{I}_n \delta(\omega - \omega_n), \quad (1)$$

where the index  $n$  labeling the vibrational modes runs from 1 to  $3N_{at}$ ,  $N_{at}$  is the total number of atoms in the model (8232 atoms),  $\omega_L$  is the frequency of the incoming photon,  $c$  is the speed of light,  $V$  is the volume of the scattering sample,  $g(\omega) = n_B(\omega) + 1$ , and  $n_B(\omega)$  is the boson factor. In experimental set-ups, it is customary to record the Raman spectra in the horizontal-horizontal

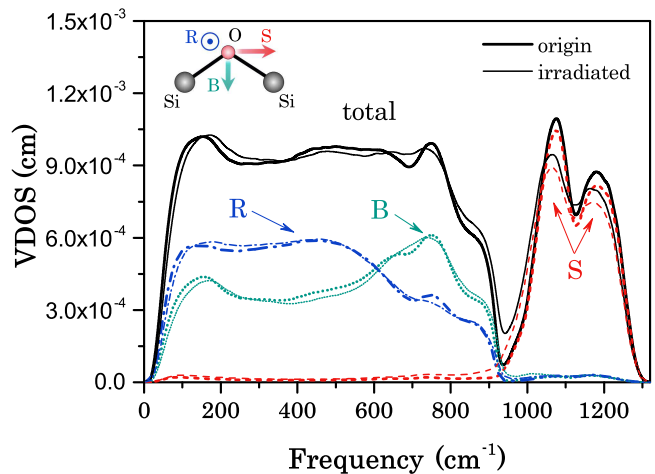


FIG. 4. The partial VDOS for the projections onto the vibrations of Si-O-Si structural units: stretching — dashed red, bending — dotted green, rocking — dash-dot blue and total — solid black. Origin sample — thick curves, after irradiation by 800 pulses — thin curves. Inset shows the relative motion of the oxygen atoms decomposed into stretching (S), bending (B), and rocking (R) components.

(HH) configuration in which the polarization of the outgoing photons is respectively parallel to the ingoing photon polarization [35]. Using the isotropy of disordered solids, we express the contribution of the  $n$ -th mode,  $\mathcal{I}_n$  to the HH-Raman spectra as [34]:

$$\mathcal{I}_n^{HH} = a_n^2 + \frac{4}{45}b_n^2, \quad (2)$$

where  $a_n$  and  $b_n$  are obtained from:

$$a_n = \frac{1}{3} \sum_i^3 \mathcal{R}_{ii}^n, \quad (3)$$

$$b_n^2 = \sum_{i<j}^3 \left\{ \frac{1}{2} (\mathcal{R}_{ii}^n - \mathcal{R}_{jj}^n)^2 + 3 (\mathcal{R}_{ij}^n)^2 \right\}. \quad (4)$$

The Raman susceptibility tensors  $\mathcal{R}_{ij}^n$  are given by [34]:

$$\mathcal{R}_{ij}^n = \sqrt{V} \sum_{I,k} \frac{\partial \chi_{ij}}{\partial R_{Ik}} \frac{\xi_{Ik}^n}{\sqrt{M_I}}, \quad (5)$$

where  $\chi$  is the electric polarizability tensor, the capital Latin indices run over the atoms, the lowercase Latin indices are the three Cartesian directions,  $\mathbf{R}_I = (R_{I1}, R_{I2}, R_{I3})$  and  $M_I$  are the position and the atomic mass of atom  $I$ , respectively. In order to compute  $\chi$ , we apply the bond polarizability model [36, 37] (see Appendix B). For a model system, the vibrational frequencies  $\omega_n^2$  and their associated eigenmodes  $\xi_I^n$  are found by solving the set of linear equations:

$$\sum_{J_j} D_{Ii, J_j} \xi_{J_j}^n = \omega_n^2 \xi_{Ii}^n, \quad (6)$$

where  $\mathbf{D}$  is the dynamical matrix, which is defined by:

$$D_{Ii,Jj} = \frac{1}{\sqrt{M_I M_J}} \frac{\partial^2 E_{tot}}{\partial R_{Ii} \partial R_{Jj}}, \text{ for } I \neq J \quad (7)$$

$$D_{Ii,Ij} = - \sum_{J \neq I} \frac{1}{M_I} \frac{\partial^2 E_{tot}}{\partial R_{Ii} \partial R_{Jj}}, \quad (8)$$

where  $E_{tot}$  is the global potential energy of the system (see Appendix A).

The result of the Raman simulations of  $v$ -SiO<sub>2</sub> are presented in Fig. 3. One can see that the main characteristics of the experimental spectra are recovered within our semi-classical approximation. In the Raman spectrum, we can recognize well the main band ( $\sim 400$ – $550$  cm<sup>-1</sup>) as well as the high-frequency bands, in particular, those located at  $\sim 800$  cm<sup>-1</sup>,  $\sim 1060$  cm<sup>-1</sup>, and  $\sim 1200$  cm<sup>-1</sup>, that are well reproduced by our simulation.

The assignment of the vibration modes of  $v$ -SiO<sub>2</sub> is well documented [38–41]. Performing projectional analysis (see Appendix C), we decompose the vibrational density of states (VDOS) for relative motions of the oxygen atoms into stretching, bending, and rocking components (see Fig. 4). The VDOS reveals pure stretching nature of the high-frequency doublet zone ( $\sim 950$ – $1300$  cm<sup>-1</sup>), the bending and rocking modes are in the range  $\sim 0$ – $900$  cm<sup>-1</sup>. In all the spectra Figs. 3 and 4, the high-frequency part of the spectra ( $\gtrsim 950$  cm<sup>-1</sup>) almost exclusively results from stretching vibrations. As far as the HH-Raman spectrum is concerned, Umari and Pasquarello showed that the bending motions dominate the rest of the spectrum ( $\sim 100$ – $900$  cm<sup>-1</sup>), whereas the contribution of rocking vibrations is suppressed with respect to their weight in the VDOS [41].

### III. RESULTS AND DISCUSSION

Comparing the experimental and modeling Raman spectra from Fig. 3, we highlight that the laser-induced changes in all bands have the same behavior. In particular, one can observe a raise and a slight shift to the right of the main band  $\omega_1$ ; the  $\omega_3$ -band has a weaker raise and a slight shift to the right. On the contrary, we can indicate the more significant changes in the high-frequency doublet zone, a shift to the left of  $\omega_2$  and  $\omega_4$  bands. In the experimental spectrum, one can see a significant gain of defect lines  $D_1$  and  $D_2$ , whereas our simulation suffers due to the lack of resolution in these areas. However, the  $D_1$  and  $D_2$  Raman defect lines are usually associated with 4- and 3-fold rings in the structure of  $v$ -SiO<sub>2</sub> [16]. Since these lines provide direct information on the concentration of these rings [43], we characterize the medium-range structure (network connectivity) by analyzing the ring distribution instead of a direct Raman analysis of the defect lines. Our previous work was dedicated to this point [5]. It is also interesting to note, that

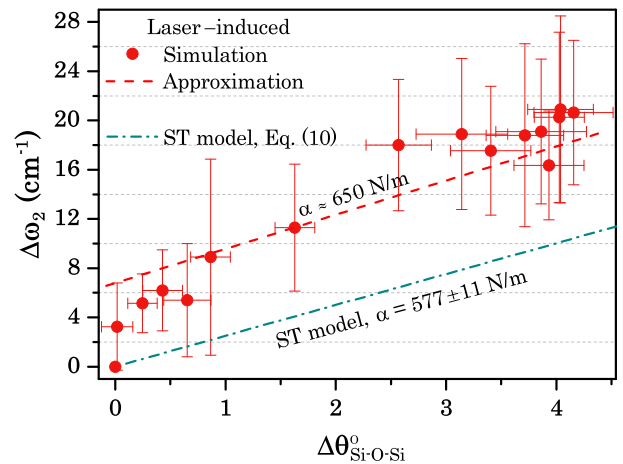


FIG. 5. Simulation of laser-induced HH-Raman  $\omega_2$ -shift versus mean Si–O–Si angle change — filled red circles (half width at half maximum fitting). The dashed red line shows the approximation of the simulation data. The results of modeling are averaged over 10 samples. The dash-dot green line shows  $\omega_2$ -shift based on the ST model [23], Eq. (10), at parameters: central-force constant  $\alpha = 577$  N/m (calculated using measured Raman characteristic frequency  $\omega_2$ , see Fig. 3) and mean Si–O–Si angle,  $\vartheta = 147.7 \pm 3.8^\circ$  [42].

the global increase in the Raman intensity in the intermediate frequency range, and the shift of the high-frequency bands in both Raman and VDOS (see Fig. 4) spectra share more similarities with the Raman and VDOS signatures of plastic-shear [22] and permanently densified glass [24, 25, 44].

In order to explain the changes in the Raman spectra upon multi-pulse laser irradiation, we exploit a simple central-force ST model to describe the dynamics of covalently bonded networks [23]. Ref. [23] assumed that the vibrations of the silica network can be described using Si–O–Si units with only one force constant  $\alpha$  defined by the Si–O bond. The following equations were proposed to describe the positions of the vibrational bands as a function of interbonding angle  $\vartheta$ :

$$\omega_1^2 = \frac{\alpha}{M_O} (1 + \cos \vartheta), \quad (9a)$$

$$\omega_2^2 = \frac{\alpha}{M_O} (1 - \cos \vartheta), \quad (9b)$$

$$\omega_3^2 = \omega_1^2 + \frac{4\alpha}{3M_{Si}}, \quad (9c)$$

$$\omega_4^2 = \omega_2^2 + \frac{4\alpha}{3M_{Si}}, \quad (9d)$$

where  $M_O$  and  $M_{Si}$  are the masses of oxygen and silicon atoms, respectively.

To extract information about the angle change from Raman spectra applying the ST model, one needs to determine the central-force constant. By using the measured Raman frequencies  $\omega_i$  (see Fig. 3) and mean Si–O–Si angle,  $\vartheta = 147.7^\circ$ , taken from [42, 45], the force

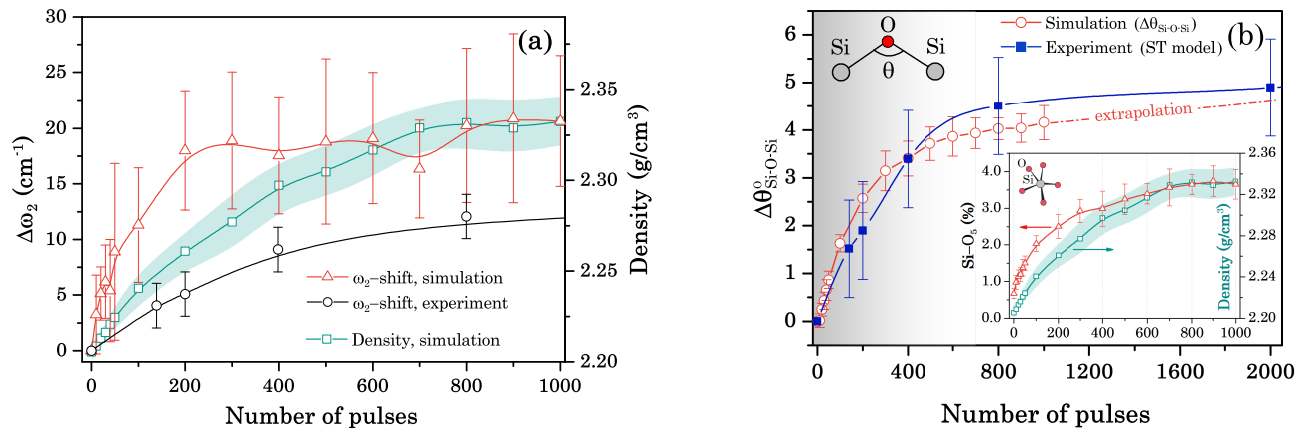


FIG. 6. (a) Absolute value  $\Delta\omega_2$  of the laser-induced HH-Raman  $\omega_2$ -shift as a function of pulse number: experiment — empty black circles; simulation — empty red triangles, compared to density change obtained in simulation — empty green squares with density dispersion depicted by the shaded green area. (b) Si–O–Si angle change versus pulse number. Experimental results via ST model — filled blue squares; results of simulation — empty red circles. Inset: Change of number of 5-coordinated Si-atoms at degree of ionization 0.018% in simulation as a function of pulse number — empty red triangles. Corresponding density — empty green squares with error bar depicted by shaded light green area. The results of modeling are averaged over 10 samples.

Force const.	$\alpha_1(\omega_1)$	$\alpha_1(\omega_g)$	$\alpha_2$	$\alpha_3$	$\alpha_4$	$\bar{\alpha}$
N/m	1170.1	710	577.3	558.8	394.0	560.0

TABLE I. Force constants.  $\bar{\alpha} = (\alpha_1(\omega_g) + \alpha_2 + \alpha_3 + \alpha_4)/4$ , where  $\alpha_{1-4}$  are calculated by Eqs. (9a)–(9d), respectively.

constants  $\alpha_{1-4}$  are calculated by Eqs. (9a)–(9d), respectively. The values of  $\alpha$  are presented in Table I. It can be seen that  $\alpha_1(\omega_1) \approx 1170$  N/m differs significantly from other values. This is probably due to a wide width of the asymmetric  $\omega_1$ -band ( $\sim 100$ – $500$   $\text{cm}^{-1}$ ) and a broad Si–O–Si angle distribution ( $\sim 135$ – $160^\circ$  [42]) that leads to an ambiguity in the calculation of  $\alpha_1$ . However, if we take instead of the frequency  $\omega_1 = 437$   $\text{cm}^{-1}$  (corresponding to the maximum of the band), the frequency  $\omega_g \approx 340$   $\text{cm}^{-1}$  corresponding to the center of gravity of the  $\omega_1$ -band, then  $\alpha_1(\omega_g) \approx 710$  N/m. Thus, all  $\alpha_{1-4}$  according to the ST model are in quite good agreement with each other.

As shown in [46], the interbonding angle change  $\Delta\vartheta$  can be related to the  $\omega_2$ -shift by differentiating Eq. (9b) to obtain:

$$\Delta\omega_2 = \frac{\alpha}{2M_O} \frac{\sin\vartheta\Delta\vartheta}{\omega_2}. \quad (10)$$

Our simulation and experimental measurements provide good resolution of the Raman  $\omega_2$ -band. Furthermore, we choose the  $\omega_2$ -band to treat the experimental measurements because the corresponding  $\alpha_2$  is closer to the mean value of central-force constant  $\bar{\alpha}$ , see Table I.

In Fig. 5 we present the simulation results of  $\omega_2$ -shift as a function of mean interbonding angle change obtained by irradiation with different number of pulses. In result, we can see that our simulations predict the linear behavior confirming the ST model, see Eq. (10). Moreover, the central-force constant values obtained from the simulation ( $\alpha \approx 650$  N/m) and calculated using the measured Raman characteristic frequency  $\omega_2$  ( $\alpha \approx 577$  N/m) are in good agreement. Thus, we demonstrate that the ST model is applicable to describe the Raman dynamics upon multiple laser irradiation.

The dynamics of  $\Delta\omega_2$  with the pulse number is shown in Fig. 6a. One can reveal two stages of dynamics, the growth during several hundreds of pulses followed by saturation, both in simulation and experiment. Despite the averaging over 10 samples, we can mention the sharp rise of the  $\omega_2$ -shift in the very beginning and noticeable dispersion in simulation that we ascribe to the size of the models (see Subsection II B). This size effect will be reduced in our further investigations by increasing the number of atoms in the samples. We can also observe two stages, growth and saturation, in the densification dynamics, that correlates quite well with the  $\omega_2$ -shift, however, it is rather smooth compared to the  $\omega_2$ -shift.

Applying the ST model to the  $\omega_2$ -shift experimental findings from Fig. 6a, we extract the corresponding angle change. One can see that the interbonding angle change follows the  $\omega_2$ -shift and also reproduces the two-stage dynamics: the growth during  $\sim 600$  pulses followed by a saturation, see Fig. 6b. The comparison shows an excellent agreement between experiment and MD simulation. Since we reveal the densification, we guess that laser-induced rearrangements should lead to transformations of  $v$ -SiO<sub>2</sub> network both in the medium-range [5] and short-range order. The short-range structure is usually

characterized by coordination number [47, 48]. We found here, a correlation between the growth of five-coordinated Si-atoms and  $v$ -SiO<sub>2</sub> densification upon laser irradiation, see inset in Fig. 6b. Similar behavior was observed in permanently densified silica glass at high pressure [47–49]. Thus, we relate the Si–O–Si angle decline to the increase of network connectivity caused by the reduction of the major ring fractions [5] and the increase in coordination defects (five-coordinated Si-atoms) due to multi-pulse laser irradiation.

#### IV. CONCLUSIONS

In summary, our systematic Raman calculation shows that upon multi-pulse laser irradiation the SiO<sub>2</sub> glass undergoes several successive transformations both in short-range and medium-range order. The changes in the Raman measurements are well described by our simulations within the numerical accuracy. This reinforces our previously developed model of bond-breaking for laser irradiation [5]. In experiment and simulation, two stages of the laser-induced densification and Raman spectrum evolution are observed: growth during several hundreds of pulses followed by further saturation. At the medium-range, the network connectivity is expressed in reduction of the major ring fractions leading to more compacted structure. By using the Raman measurements and the ST model, we highlight the short-range transformation by extracting the dynamics of Si–O–Si angle change. These results are in excellent agreement with our simulation results. In addition, we show a correlation between the growth of five-coordinated Si-atoms and densification due to laser irradiation. Thus, we conclude that the laser-induced densification of  $v$ -SiO<sub>2</sub> is related to the changes in the short-range order caused by the appearance of Si-coordination defects and medium-range order connected to evolution of the ring distribution. These findings disclose similarities between laser-induced- and permanently-densified glass [19, 21]. Moreover, our preliminary analysis shows more generally that the sensitivity of the Raman spectra to pressure variation depends strongly on the samples preparation protocol. We also note that the global increase in the Raman intensity in the intermediate frequency range, and the shift of the high-frequency bands share more similarities with the Raman signature of plastic-shear [22]. Therefore, our simulation results suggest interesting future experiment in order to clarify the impact of the thermo-mechanical history on glasses under shear, cold- and hot-compression, and laser-induced densification.

#### ACKNOWLEDGMENTS

M.E. Povarnitsyn was supported by the Russian Science Foundation, grant No. 16-19-10700. The authors thank LaHC (Saint-Etienne) and ILM (Lyon) for stimu-

lating discussions, and Intel team (G. Fedorov, V. Chumakov and I. Sokolova) for support with the FEAST Eigenvalue Solver. N.S. Shcheblanov and A. Tanguy acknowledge the French Research National Agency program ANR MECASIL (ANR-12-BS04-0004) and BQR financing from LaMCoS.

#### Appendix A: BKS<sub>W</sub> potential

The equilibration of the liquid, quench and relaxation of the glass are performed classically using the BKS<sub>W</sub> potential [33], which is a modified version of the van Beest, Kramer and van Santen (BKS) potential [32]. It can be described as a two-body potential:

$$\Phi_{\alpha\beta}^{BKS<sub>W</sub>}(R) = \Phi_{\alpha\beta}^{Coul}(R) + \Phi_{\alpha\beta}^{Buck}(R), \quad (A1)$$

where  $\alpha$  and  $\beta$  are the types of atoms (O or Si), and  $R$  is the distance between them.

$$\Phi_{\alpha\beta}^{Coul}(R) = q_{\alpha}q_{\beta}e^2V_W(R)G_W(R), \quad (A2)$$

with

$$V_W(R) = \left(\frac{1}{R} - \frac{1}{R_{c,W}}\right) + \frac{1}{R_{c,W}^2}(R - R_{c,W}), \quad (A3)$$

$$G_W(R) = \exp\left(-\frac{\gamma_W^2}{(R - R_{c,W})^2}\right). \quad (A4)$$

$$\Phi_{\alpha\beta}^{Buck}(R) = \left[ A_{\alpha\beta} \left( e^{-\frac{R}{\rho_{\alpha\beta}}} - e^{-\frac{R_{c,sh}}{\rho_{\alpha\beta}}} \right) - C_{\alpha\beta} \left( \frac{1}{R^6} - \frac{1}{R_{c,sh}^6} \right) \right] G_{sh}(R), \quad (A5)$$

with

$$G_{sh}(R) = \exp\left(-\frac{\gamma_{sh}^2}{(R - R_{c,sh})^2}\right), \quad (A6)$$

where  $\gamma_{sh} = \gamma_W = 0.5 \text{ \AA}$ ,  $R_{c,W} = 10.17 \text{ \AA}$ , and  $R_{c,sh} = 5.5 \text{ \AA}$ . We also add a strong and regular repulsive part at short range ( $R < R_{inf}$ ) to avoid the collapse of atoms at high pressure, or high temperatures. The added repulsive part has the following form:

$$\Phi_{\alpha\beta}^{Rep}(R) = \left(\frac{D_{\alpha\beta}}{R}\right)^{12} + E_{\alpha\beta}R + F_{\alpha\beta}. \quad (A7)$$

$D_{\alpha\beta}$ ,  $E_{\alpha\beta}$ , and  $F_{\alpha\beta}$  have been adjusted in order to have the continuity of the potential and its first, and second derivatives. The parameters of this potential are tabulated in Table II. The total energy, which is used to compute the Dynamical Matrix, can be written:

$$E_{tot} = \sum_{I < J} \Phi_{\alpha_I\beta_J}^{BKS<sub>W</sub>}(R) + \Phi_{\alpha_I\beta_J}^{Rep}(R), \quad (A8)$$

and here  $R$  is the distance between atoms  $I$  and  $J$ .

	$A_{\alpha\beta}$ (eV)	$\rho_{\alpha\beta}$ (Å)	$C_{\alpha\beta}$ (eV·Å <sup>6</sup> )	$D_{\alpha\beta}$ (Å·eV <sup>-12</sup> )
O-O	1388.773	0.3623	175.0	1.51166281
Si-O	18003.7572	0.2052	133.5381	1.42402882
Si-Si	872360308.1	0.0657	23.299907	0.0

	$E_{\alpha\beta}$ (eV·Å <sup>-1</sup> )	$F_{\alpha\beta}$ (eV)	$R_{inf}$ (Å)
O-O	-14.97811134	39.0602602165	1.75
Si-O	-3.24749265	-15.86902056	1.27
Si-Si	0.0	0.0	0.0

TABLE II. Parameters of the empirical potential used to model the silica glass.

### Appendix B: Bond polarizability model

The bond polarizability model (BPM) [36, 37] has successfully been applied for the calculation of Raman intensities in a large variety of systems [34]. In this approach, the polarizability is modeled in terms of bond contributions:

$$\chi_{ij}(I) = \frac{1}{V} \sum_J \alpha_{ij}(I, J), \quad (\text{B1})$$

where the polarizability tensors  $\alpha_{ij}(I, J)$ :

$$\alpha_{ij} = \frac{1}{3}(2\alpha_p + \alpha_l)\delta_{ij} + (\alpha_l - \alpha_p) \left( \frac{R_i R_j}{|\mathbf{R}|^2} - \frac{1}{3}\delta_{ij} \right), \quad (\text{B2})$$

where  $\mathbf{R} = \mathbf{R}_I - \mathbf{R}_J$  is a vector which defines the direction and the distance of a pair of nearest neighbor atoms at sites  $\mathbf{R}_I$  and  $\mathbf{R}_J$ . The parameters  $\alpha_l$  and  $\alpha_p$  correspond to the longitudinal and perpendicular bond polarizability, respectively.

The BPM further assumes that the bond polarizabilities  $\alpha_l$  and  $\alpha_p$  only depend on the length of the bond. Thus the derivative of the local bond polarizability with respect to the relative displacement of the atoms  $I$  and  $J$  yields:

$$\begin{aligned} \frac{\partial \alpha_{ij}(I, J)}{\partial R_{Ik}} &= \frac{1}{3} (2\alpha'_p + \alpha'_l) \delta_{ij} \hat{R}_k \\ &+ (\alpha'_l - \alpha'_p) \left( \hat{R}_i \hat{R}_j - \frac{1}{3}\delta_{ij} \right) \hat{R}_k \\ &+ \frac{(\alpha_l - \alpha_p)}{R} \left( \delta_{ik} \hat{R}_j + \delta_{jk} \hat{R}_i - 2\hat{R}_i \hat{R}_j \hat{R}_k \right), \quad (\text{B3}) \end{aligned}$$

where  $\hat{\mathbf{R}}$  is a unit vector along  $\mathbf{R}$ ,  $\alpha'_l$  and  $\alpha'_p$  are the derivatives of the bond polarizabilities with respect to the bond length ( $\alpha'_{l,p} = (\partial \alpha_{l,p} / \partial R)|_{R=R_0}$  and  $R_0$  is a typical distance). Therefore, when one type of bond occurs, the BPM is completely defined by three parameters:  $2\alpha'_p + \alpha'_l$ ,  $\alpha'_l - \alpha'_p$ , and  $(\alpha_l - \alpha_p)/R$ . We use the parameters of the BPM already derived in Refs. [50, 51], whose values are summarized in Table III.

Parameter	$2\alpha'_p + \alpha'_l$	$\alpha'_l - \alpha'_p$	$(\alpha_l - \alpha_p)/R$
$(4\pi)^{-1} \cdot \text{Bohr}^{-1}$	0.771	0.196	0.056

TABLE III. Bond polarizability model parameters.

### Appendix C: Vibrational density of states

The frequencies  $\omega_n^2$  and the corresponding normalized eigenmodes  $\xi_I^n$  are obtained by diagonalizing the dynamical matrix. The FEAST solver integrated into Intel MKL is used for the diagonalization [52]. The associated atomic displacements are given by:

$$\mathbf{u}_I^n = \frac{\xi_I^n}{\sqrt{M_I}}. \quad (\text{C1})$$

The index  $n$  labeling the vibrational modes runs from 1 to  $3N_{at}$ ,  $N_{at}$  is the total number of atoms in the model.

The structure of *v*-SiO<sub>2</sub> consists of corner-shared tetrahedral SiO<sub>4</sub> units. These units are connected to each other via bridging oxygen atoms. Since oxygen vibrations give the prominent contribution to the Raman spectra, we further decompose this contribution according to three orthogonal directions which characterize the local environment of each oxygen atom [53]. Considering the plane containing the silicon atoms to which a given oxygen atom is bonded, we defined the three directions as in [53, 54]. We took the first direction orthogonal to the Si–O–Si plane (rocking), the second one along the bisector of the Si–O–Si angle (bending), and the third one orthogonal to the two previous ones (stretching), see the sketch in Fig. 4. The decomposition is carried out by projecting the displacements  $\mathbf{u}_I^n$  onto these directions prior to the calculation of the VDOS spectra, i.e.  $\mathbf{u}_I^n = \mathbf{u}_{I_r}^n + \mathbf{u}_{I_b}^n + \mathbf{u}_{I_s}^n$  and related to rocking ( $\mathbf{u}_{I_r}^n$ ), bending ( $\mathbf{u}_{I_b}^n$ ), and stretching ( $\mathbf{u}_{I_s}^n$ ) motions. Bearing in mind that the two silicon atoms Si<sub>1(I)</sub> and Si<sub>2(I)</sub> that are neighbors of the oxygen atom  $I$  move as well, only the relative motion of the oxygen atom is decomposed, so that  $\tilde{\mathbf{u}}_I^n = \mathbf{u}_I^n - (\mathbf{u}_{\text{Si}_1(I)}^n + \mathbf{u}_{\text{Si}_2(I)}^n)/2$  is the displacement of oxygen atom  $I$  relative to the average displacement of its nearest silicon neighbors. Total VDOS decomposes  $Z(\omega)$  into the stretching, bending, and rocking components,  $Z(\omega) = Z_r(\omega) + Z_b(\omega) + Z_s(\omega)$ :

$$Z_{r,b,s}(\omega) = \frac{1}{3N_{at}} \sum_n |\tilde{r}^n|_{r,b,s}^2 \delta(\omega - \omega_n), \quad (\text{C2})$$

where the squared average displacement can be calculated according to the following expression:

$$|\tilde{r}^n|_{r,b,s}^2 = \frac{1}{\sum_I |\tilde{\mathbf{u}}_I^n|^2} \sum_I |\tilde{\mathbf{u}}_I^n|_{r,b,s}^2, \quad (\text{C3})$$

where  $N_O$  is the number of oxygen atoms.

- [1] R. R. Gattass and E. Mazur, *Femtosecond laser micromachining in transparent materials*, Nat. Photonics **2**, 219 (2008).
- [2] M. Ams, G. D. Marshall, P. Dekker, J. A. Piper, and M. J. Withford, *Ultrafast laser written active devices*, Laser Photon. Rev. **3**, 535 (2009).
- [3] M. Malinauskas, A. Žukauskas, S. Hasegawa, Y. Hayasaki, V. Mizeikis, R. Buividas, and S. Juodkazis, *Ultrafast laser processing of materials: from science to industry*, Light: Sci. Appl. **5**, e16133 (2016).
- [4] Y. Bellouard, E. Barthel, A. A. Said, M. Dugan, and P. Bado, *Scanning thermal microscopy and Raman analysis of bulk fused silica exposed to low-energy femtosecond laser pulses*, Opt. Express **16**, 19520 (2008).
- [5] N. S. Shcheblanov and M. E. Povarnitsyn, *Bond-breaking mechanism of vitreous silica densification by IR femtosecond laser pulses*, EPL (Europhys. Lett.) **114**, 26004 (2016).
- [6] A. Zoubir, C. Rivero, R. Grodsky, K. Richardson, M. Richardson, T. Cardinal, and M. Couzi, *Laser-induced defects in fused silica by femtosecond IR irradiation*, Phys. Rev. B **73**, 224117 (2006).
- [7] Y. Shimotsuna, M. Sakakura, and K. Miura, *Manipulation of optical anisotropy in silica glass*, Opt. Mater. Express **1**, 803 (2011).
- [8] J. W. Chan, T. Huser, S. Risbud, and D. M. Krol, *Structural changes in fused silica after exposure to focused femtosecond laser pulses*, Opt. Lett. **26**, 1726 (2001).
- [9] C. W. Ponader, J. F. Schroeder, and A. M. Streltsov, *Origin of the refractive-index increase in laser-written waveguides in glasses*, J. Appl. Phys. **103**, 063516 (2008).
- [10] K. Mishchik, C. D'Amico, P. K. Velpula, C. Mauclair, A. Boukenter, Y. Ouerdane, and R. Stoian, *Ultrafast laser induced electronic and structural modifications in bulk fused silica*, J. Appl. Phys. **114**, 133502 (2013).
- [11] R. Stoian, K. Mishchik, G. Cheng, C. Mauclair, C. D'Amico, J.-P. Colombier, and M. Zamfirescu, *Investigation and control of ultrafast laser-induced isotropic and anisotropic nanoscale-modulated index patterns in bulk fused silica*, Opt. Mat. Express **3**, 1755 (2013).
- [12] Y. Bellouard, A. Champion, B. McMillen, S. Mukherjee, R. R. Thomson, C. Pépin, P. Gillet, and Y. Cheng, *Stress-state manipulation in fused silica via femtosecond laser irradiation*, Optica **3**, 1285 (2016).
- [13] R. Stoian, C. D'Amico, M. Bhuyan, and G. Cheng, *Ultrafast laser photoinscription of large-mode-area waveguiding structures in bulk dielectrics: Invited paper for the section: Hot topics in ultrafast lasers*, Opt. Laser Technol. **80**, 98 (2016).
- [14] J. Hernandez-Rueda, J. Clarijs, D. van Oosten, and D. M. Krol, *The influence of femtosecond laser wavelength on waveguide fabrication inside fused silica*, Appl. Phys. Lett. **110**, 161109 (2017).
- [15] R. A. Barrio, F. L. Galeener, E. Martinez, and R. J. Elliott, *Regular ring dynamics in AX<sub>2</sub> tetrahedral glasses*, Phys. Rev. B **48**, 15672 (1993).
- [16] A. Pasquarello and R. Car, *Identification of Raman defect lines as signatures of ring structures in vitreous silica*, Phys. Rev. Lett. **80**, 5145 (1998).
- [17] P. Y. Huang, S. Kurasch, J. S. Alden, A. Shekhawat, A. A. Alemi, P. L. McEuen, J. P. Sethna, U. Kaiser, and D. A. Muller, *Imaging atomic rearrangements in two-dimensional silica glass: Watching silica's dance*, Science **342**, 224 (2013).
- [18] M. Bressel, D. de Ligny, C. Sonnevile, V. Martinez, V. Mizeikis, R. Buividas, and S. Juodkazis, *Femtosecond laser induced density changes in GeO<sub>2</sub> and SiO<sub>2</sub> glasses: fictive temperature effect*, Opt. Mat. Express **1**, 605 (2011).
- [19] T. Deschamps, J. Margueritat, C. Martinet, A. Mermet, and B. Champagnon, *Elastic moduli of permanently densified silica glasses*, Sci. Rep. **4**, 7193 (2014).
- [20] C. Martinet, A. Kassir-Bodon, T. Deschamps, A. Cornet, S. Le Floch, V. Martinez, and B. Champagnon, *Permanently densified SiO<sub>2</sub> glasses: a structural approach*, J. Phys.: Condens. Mat. **27**, 325401 (2015).
- [21] A. Cornet, V. Martinez, D. de Ligny, B. Champagnon, and C. Martinet, *Relaxation processes of densified silica glass*, J. Chem. Phys. **146**, 094504 (2017).
- [22] N. S. Shcheblanov, B. Mantis, P. Umari, and A. Tanguy, *Detailed analysis of plastic shear in the Raman spectra of SiO<sub>2</sub> glass*, J. Non-Cryst. Solids **428**, 6 (2015).
- [23] P. N. Sen and M. F. Thorpe, *Phonons in AX<sub>2</sub> glasses: From molecular to band-like modes*, Phys. Rev. B **15**, 4030 (1977).
- [24] B. Hehlen, *Inter-tetrahedra bond angle of permanently densified silicas extracted from their Raman spectra*, J. Phys.: Condens. Mat. **22**, 025401 (2010).
- [25] C. Weigel, M. Foret, B. Hehlen, M. Kint, S. Clement, A. Polian, R. Vacher, and B. Rufflé, *Polarized Raman spectroscopy of v-SiO<sub>2</sub> under rare-gas compression*, Phys. Rev. B **93**, 224303 (2016).
- [26] S. M. Eaton, H. Zhang, M. L. Ng, J. Li, W.-J. Chen, S. Ho, and P. R. Herman, *Transition from thermal diffusion to heat accumulation in high repetition rate femtosecond laser writing of buried optical waveguides*, Opt. Express **16**, 9443 (2008).
- [27] K. Sugioka and Y. Cheng, *Ultrafast lasers—reliable tools for advanced materials processing*, Light: Sci. Appl. **3**, e149 (2014).
- [28] W. H. Zachariasen, *The atomic arrangement in glass*, J. Am. Chem. Soc. **54**, 3841 (1932).
- [29] B. Mantisi, A. Tanguy, G. Kermouche, and E. Barthel, *Atomistic response of a model silica glass under shear and pressure*, Eur. Phys. J. B **85**, 1 (2012).
- [30] S. Plimpton, *Fast parallel algorithms for short-range molecular dynamics*, J. Comput. Phys. **117**, 1 (1995).
- [31] K. Binder and W. Kob, *Glassy materials and disordered solids: An introduction to their statistical mechanics* (World Scientific, Singapore, 2011).
- [32] B. W. H. van Beest, G. J. Kramer, and R. A. van Santen, *Force fields for silicas and aluminophosphates based on ab initio calculations*, Phys. Rev. Lett. **64**, 1955 (1990).
- [33] A. Carré, L. Berthier, J. Horbach, S. Ispas, and W. Kob, *Amorphous silica modeled with truncated and screened Coulomb interactions: A molecular dynamics simulation study*, J. Chem. Phys. **127**, 114512 (2007).
- [34] M. Cardona and G. Guentherodt, *Light Scattering in Solids II* (Springer-Verlag, 1982).
- [35] P. Bruesch, *Phonons: Theory and Experiments. Vol. 2* (Springer, Berlin, 1986).

- [36] M. W. Wolkenstein, *Intensities of vibrational spectra of molecules*, C. R. Acad. Sci. URSS **30**, 791 (1941).
- [37] M. Eliashevich and M. Wolkenstein, *The theory of intensities and polarization of vibration spectra of molecules*, J. Phys. USSR **9**, 101 (1945).
- [38] S. N. Taraskin and S. R. Elliott, *Nature of vibrational excitations in vitreous silica*, Phys. Rev. B **56**, 8605 (1997).
- [39] N. S. Shcheblanov, M. E. Povarnitsyn, S. N. Taraskin, and S. R. Elliott, *Addendum and Erratum: Nature of vibrational excitations in vitreous silica [Phys. Rev. B 56, 8605 (1997)]*, Phys. Rev. B **94**, 099903 (2016).
- [40] J. Sarnthein, A. Pasquarello, and R. Car, *Origin of the high-frequency doublet in the vibrational spectrum of vitreous SiO<sub>2</sub>*, Science **275**, 1925 (1997).
- [41] P. Umari and A. Pasquarello, *First-principles analysis of the Raman spectrum of vitreous silica: comparison with the vibrational density of states*, J. Phys.: Condens. Mat. **15**, S1547 (2003).
- [42] N. M. Trease, T. M. Clark, P. J. Grandinetti, J. F. Stebbins, and S. Sen, *Bond length-bond angle correlation in densified silica—Results from <sup>17</sup>O NMR spectroscopy*, J. Chem. Phys. **146**, 184505 (2017).
- [43] P. Umari, X. Gonze, and A. Pasquarello, *Concentration of small ring structures in vitreous silica from a first-principles analysis of the Raman spectrum*, Phys. Rev. Lett. **90**, 027401 (2003).
- [44] A. Hiramatsu, M. Arai, H. Shibazaki, M. Tsunekawa, T. Otomo, A. C. Hannon, S. M. Bennington, N. Kitamura, and A. Onodera, *Investigation on permanently densified vitreous silica by means of neutron scattering*, Physica B **219-220**, 287 (1996).
- [45] W. J. Malfait, W. E. Halter, and R. Verel, *<sup>29</sup>Si NMR spectroscopy of silica glass: T<sub>1</sub> relaxation and constraints on the Si–O–Si bond angle distribution*, Chem. Geol. **256**, 269 (2008).
- [46] A. Geissberger and F. L. Galeener, *Raman studies of vitreous SiO<sub>2</sub> versus fictive temperature*, Phys. Rev. B **28**, 3266 (1983).
- [47] A. Trave, P. Tangney, S. Scandolo, A. Pasquarello, and R. Car, *Pressure-induced structural changes in liquid SiO<sub>2</sub> from ab initio simulations*, Phys. Rev. Lett. **89**, 245504 (2002).
- [48] A. Zeidler, K. Wezka, R. F. Rowlands, D. A. Whittaker, P. S. Salmon, A. Polidori, J. W. Drewitt, S. Klotz, H. E. Fischer, M. C. Wilding, C. L. Bull, M. G. Tucker, and M. Wilson, *High-pressure transformation of SiO<sub>2</sub> glass from a tetrahedral to an octahedral network: a joint approach using neutron diffraction and molecular dynamics*, Phys. Rev. Lett. **113**, 135501 (2014).
- [49] C. Benmore, E. Soignard, S. Amin, M. Guthrie, S. Shastri, P. Lee, and J. Yarger, *Structural and topological changes in silica glass at pressure*, Phys. Rev. B **81**, 054105 (2010).
- [50] P. Umari, A. Pasquarello, and A. Dal Corso, *Raman scattering intensities in  $\alpha$ -quartz: A first-principles investigation*, Phys. Rev. B **63**, 094305 (2001).
- [51] L. Giacomazzi, P. Umari, and A. Pasquarello, *Medium-range structure of vitreous SiO<sub>2</sub> obtained through first-principles investigation of vibrational spectra*, Phys. Rev. B **79**, 064202 (2009).
- [52] Intel Corporation, Intel Math Kernel Library, <https://software.intel.com/en-us/intel-mkl>.
- [53] R. Bell, *The dynamics of disordered lattices*, Rep. Prog. Phys. **35**, 1315 (1972).
- [54] A. Pasquarello, J. Sarnthein, and R. Car, *Dynamic structure factor of vitreous silica from first principles: Comparison to neutron-inelastic-scattering experiments*, Phys. Rev. B **57**, 14133 (1998).